Invited Articles

Impact dynamics of droplet containing particle suspensions on deep liquid pool

Boqian Yan [1] and Xiaoyu Tang [1,2,*]
[1]Department of Mechanical and Industrial Engineering, Northeastern University, Boston, Massachusetts 02115, USA
[2]Department of Chemical Engineering, Northeastern University, Boston, Massachusetts 02115, USA

(Received 12 March 2026; accepted 29 May 2026; published 22 June 2026)

Droplets impacting on liquid pools have been extensively studied because of their complex dynamics and relevance to many natural and industrial processes. However, most of the research has focused on droplets of Newtonian fluids, and much less is known about droplets containing suspension particles, which adds another layer of complexity of non-Newtonian effect. To address this gap, we studied droplets containing cornstarch particles impacting a deep water pool over a range of impact velocities u_0 (0.5–3 m/s) and particle volume fractions ϕ (36.8–47.5%). We identified five distinct impact phenomena, several of which are absent in the impacts of Newtonian droplets, and collected them in a regime map in the nondimensional space of Weber number and ϕ. Through an energy-based scaling analysis, we elucidated the origins of and transitions between these phenomena, revealing that the competition between the pool cavity dynamics and the rheological properties of the suspension is the key factor governing the observed impact behaviors. Our results deepen the understanding of the complex interplay between impact dynamics, cavity evolution, and suspension rheology, offering practical guidance for a range of engineering applications.

DOI: 10.1103/fxw2-38g4

I. INTRODUCTION

The impact of droplets on a liquid pool plays a crucial role in many engineering and manufacturing processes [1–12]. The interplay of inertial, viscous, and capillary forces produces a range of outcomes, such as bouncing [13–19], spreading [20–25], and splashing [26–32]. By controlling these dynamics, engineers can manipulate the mass transfer between the droplet and the pool to improve both the yield and the product quality. However, in many applications, such as material fabrication [33], droplets contain particles for additional functionality. The suspension droplets often exhibit non-Newtonian behaviors [34–36], such as viscoelasticity, shear thinning, and shear thickening, adding rheological complexity to the impact dynamics. On the other hand, the impact process generates complex flow fields inside the droplet and within the pool, which redistribute the particles and create heterogeneous viscosity distributions. Therefore, a thorough investigation of suspension droplets impact dynamics not only guides practical applications but also advances our fundamental knowledge of suspension behaviors in complex flow fields, shedding light on phenomena such as impact-induced jamming [37–39].

The impact dynamics of suspension droplets on solid substrates have been studied both experimentally [40–42] and numerically [43], revealing unique phenomena compared to Newtonian droplet impact. Boyer *et al.* [41] showed that the final deformation of the droplet is insensitive

*Contact author: x.tang@northeastern.edu

TABLE I. Range of weight percentage and volume fraction of the cornstarch suspensions tested in this work.

Weight percentage (wt.%)	30.0	31.0	32.0	33.0	34.0	35.0	36.0	37.0	38.0	39.0
Volume fraction ϕ (%)	36.8	38.0	39.2	40.4	41.6	42.8	44.0	45.2	46.3	47.5

to the initial impact velocity due to the suspension rheology with Bagnoldian relationship. Shah *et al.* [40,44] demonstrated that, at high particle volume fractions, droplets behave like elastic solid spheres and the jamming occurs within milliseconds after the initial contact. They also observed the coexistence of liquid and solid phases at intermediate volume fractions. These studies on the impacts of suspension droplets on a solid substrate unveiled the rich physics stemming from the coupling between suspension rheology and droplet impact. Moreover, the impact on a liquid pool adds another layer of complexity and remains less explored. A liquid surface can deform upon droplet impact which may provide less stress to the suspension, while the droplet can penetrate the pool and release the particles to the liquid to interact with the resulting flow field. These unique features raise key questions: What impact phenomena would emerge when suspension droplets impact on liquid pools and how do their rheological properties influence such behaviors?

To address these questions, we investigated the impact dynamics of cornstarch suspension droplets on a deep water pool using high-speed imaging and rheological characterization. By varying the impact velocity u_0 and particle volume fraction ϕ of the droplets, we identified impact phenomena that are unique in the suspension droplets impact on liquid pool, such as *wrapped bubble* and *solid lump*, and organized those in a regime map of Weber number and the particle volume fraction. We examined and unveiled how non-Newtonian behavior competes with impact inertia and capillarity in setting the observed outcomes. By combining rheological measurements and energy balance analysis, we identified theoretical predictions for the transition boundaries between different regimes, thus providing guidelines for selecting conditions to obtain desired impact outcomes for practical applications. Overall, this work provides a framework for interpreting and predicting the impact dynamics of suspension droplets on deformable liquid surfaces and highlights the role of suspension rheology in shaping droplet-pool coupling and regime transitions.

II. METHODS

A. Materials and characterization

The suspension fluid is composed of cornstarch particles (Sigma Aldrich) with density $\rho_c = 1630\,\mathrm{kg/m^3}$ and a solution of 55 wt.% cesium chloride (CsCl, Sigma Aldrich) in DI water. The density of the suspending liquid matches that of the particle such that the suspension remains stable and uniformly distributed for up to a week. Cornstarch particles are relatively monodisperse with a characteristic diameter of 14 μm [45] and Brownian motion can be neglected [46]. In this work, we report the concentration of cornstarch particles in terms of the volume fraction ϕ (Table I) rather than the mass fraction because the rheological properties of suspensions are primarily reported by their particle volume fractions. The conversion from mass fraction to volume fraction follows Han *et al.* [47], which is detailed in Sec. S1 in Supplementary Material [48]. The volume fraction of the cornstarch particles used in the droplet impact experiments ranges from 36.8% to 47.5%, which are below the jamming threshold $\phi_J = 52.0\%$, tested during sample preparation.

Rheological properties of suspensions at various volume fractions were measured using a DHR-3 rheometer (TA Instruments) in a parallel-plate configuration (40-mm plate diameter, 500 μm gap). A logarithmically spaced shear-rate sweep was applied from 1 to 5000 $\mathrm{s^{-1}}$ and the corresponding shear stress was recorded. The results and interpretations will be discussed in Sec. III B.

The surface tension of the cornstarch suspension σ_d was measured using the pendant drop method [49,50] at different volume fractions ϕ and is shown in Fig. 1. There is no significant change in σ_d

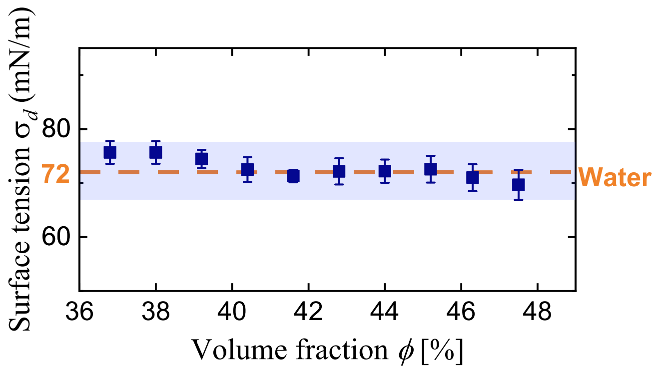

FIG. 1. Surface tension measurement of the cornstarch suspension σ_d with various volume fractions ϕ by the pendant drop method. The blue shaded area highlights the range of σ_d with all ϕ. The orange dash line marks the value of surface tension of DI water.

with varying ϕ, and the values hover around the value of water σ_w, indicated by the orange dashed line. Thus, both σ_d and σ_w are denoted as σ, with the value $\sigma = 72$ mN/m for subsequent analysis.

B. Experimental setup and procedure

To prepare the suspension fluid, cornstarch particles were mixed with the CsCl solution using a glass stirrer and the mixture was sonicated (Branson 8510) for 10 min. The suspension was then transferred to a syringe connected to a needle (Gauge 18, McMaster-Carr). To ensure consistent results, each batch of suspension fluid was used within 3 hours of preparation. As shown in Fig. 2, the syringe was mounted on a syringe pump (New Era), which delivered the fluid at a low constant flow rate. Droplets were detached from the needle once their weight exceeded the capillary force at the tip of the needle and fell on a water pool in a cubic container ($50 \times 50 \times 50$ mm^3). The suspension droplets remain spherical prior to the impact, and their diameter D ranges from 2.8 to 3.2 mm for all volume fractions, as shown in Fig. S1(a) in Supplemental Material [48]. The large pool height $H = 50$ mm ($H/D > 10$) ensures that the container substrate does not affect impact dynamics [17]. The impact velocity was controlled by varying the needle height above the pool from 3 to 400 mm, which gives a velocity ranging from 0.5 to 3 m/s. A high-speed camera (Phantom VEO 1310, Vision Research) recorded the side-view images of each impact at 10 000 fps with front lighting.

C. Image processing

The images were postprocessed with customized MATLAB codes to extract key parameters such as the droplet diameter D and the impact velocity u_0. u_0 is obtained by extracting the slope of a linear fit of the center positions y of the droplet versus time t, as shown in Fig. S1(b) in Supplemental Material [48], which confirms that the droplets fall at a constant velocity u_0 prior to impact.

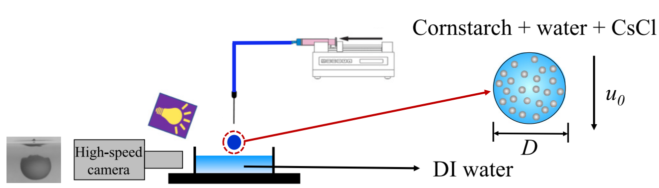

FIG. 2. Experimental configuration for studying cornstarch suspension droplets impact on a water pool.

The positions of the top and bottom points of the droplet are also tracked from the moment of first contact until full immersion in the pool to monitor the deformation as the droplet penetrates through the liquid surface, as shown in Fig. S2 in Supplemental Material [48]. The linear behavior at each stage for each line confirms the constant velocities of the top and bottom of the droplet during penetration. By linear fitting of each position versus time, the velocities of the top u_{top} and bottom u_{bot} are extracted.

III. RESULTS

A. Impact phenomenology

Figure 3 shows five distinct impact dynamics of cornstarch suspension droplets on a water pool at various u_0 and volume fractions ϕ. At low u_0 (0.85 m/s) and ϕ (36.8%) as shown in Fig. 3(a), the suspension droplet merges with the liquid pool upon impact, detaches from the cavity, and the mass (solution and cornstarch particles) from the droplet continues to descend due to inertia. Once the top surface of the droplet moves below the original pool surface, the cavity forms and starts to grow and interact with the mass from the droplet. While the cavity retracts due to the capillary effect, the mass from the droplet continues to descend, forming a liquid lump that can be distinguished from the liquid pool. This regime is named *liquid lump*. At higher u_0 (1.41 m/s) with the same ϕ as shown in Fig. 3(b), more kinetic energy in the droplet converts to more energy in the cavity, leading to a stronger interaction with the mass from the droplet. The mass from the droplet is partially dispersed and wrapped around part of the cavity, but the bottom portion of the droplet remains together in a hemispherical shape, as the cavity grows downward in a cylindrical fashion. This regime is named *partially attached*, emphasizing the intermediate effect of the interaction between the cavity and the mass from the droplet. At even higher u_0 (2.07 m/s) as shown in Fig. 3(c), the cavity gains so much more energy from the suspension droplet that it expands spherically dominated by the inertia effect. The mass from the droplet is fully dispersed into a hemispherical shell and wraps around the entire cavity. This regime is named *fully attached*. The quantitative distinction between the partially attached and fully attached regimes is determined from the experimental measurement of the evolution of the cavity shape, with the details provided in Sec. S3 in Supplemental Material [48]. It is noted that the cavity behaviors in these three regimes are similar to those of Newtonian droplets: With increasing impact speed, the cavity size grows, and its shape transitions from cone to hemisphere. Snapshots for water droplet impact are shown in Fig. S4 in Supplemental Material [48] for qualitative comparison.

Distinctive phenomena emerge at higher volume fraction ϕ. At similar u_0 (1.45 m/s) as in the partially attached case ($\phi = 36.8\%$), wrapped bubble occurs at $\phi = 41.6\%$, as shown in Fig. 3(d), and solid lump is observed at $\phi = 47.5\%$, as shown in Fig. 3(e). For the wrapped bubble case, the cavity becomes unstable shortly after the impact, in contrast to the continuous expansion in previous cases. The lower section of the mass from the droplet remains undisturbed, descending as a cohesive lump; while the upper section of the mass from the droplet wraps around the cavity, eventually pulls one or more bubbles from the cavity and brings them down together with the droplet mass. The bubble formation mechanism differs fundamentally from that in Newtonian droplet impacts, as we will discuss in Sec. IV B. For the solid lump case, the entire mass from the droplet descends as a whole, maintaining an almost unchanged shape. In addition, minimal cavity formation is observed throughout the impact process, which resembles the impact of hydrophilic solid balls on liquid surfaces [51–54].

In both high ϕ cases, the mass from the droplet exhibits jamming behavior. The jamming transition has been observed for the impact of suspension droplets on solid surfaces, manifested as limited deformation [41,44]. To validate the jamming transition at high volume fractions, the vertical length of the droplets, $L(t)$, is measured from the moment of first contact with the pool surface to full immersion. Figure 4 presents the normalized vertical length L/D as a function of the normalized time $\tau = tu_0/D$. At $\phi = 38.0\%$, L/D decreases monotonically, indicating a continuous

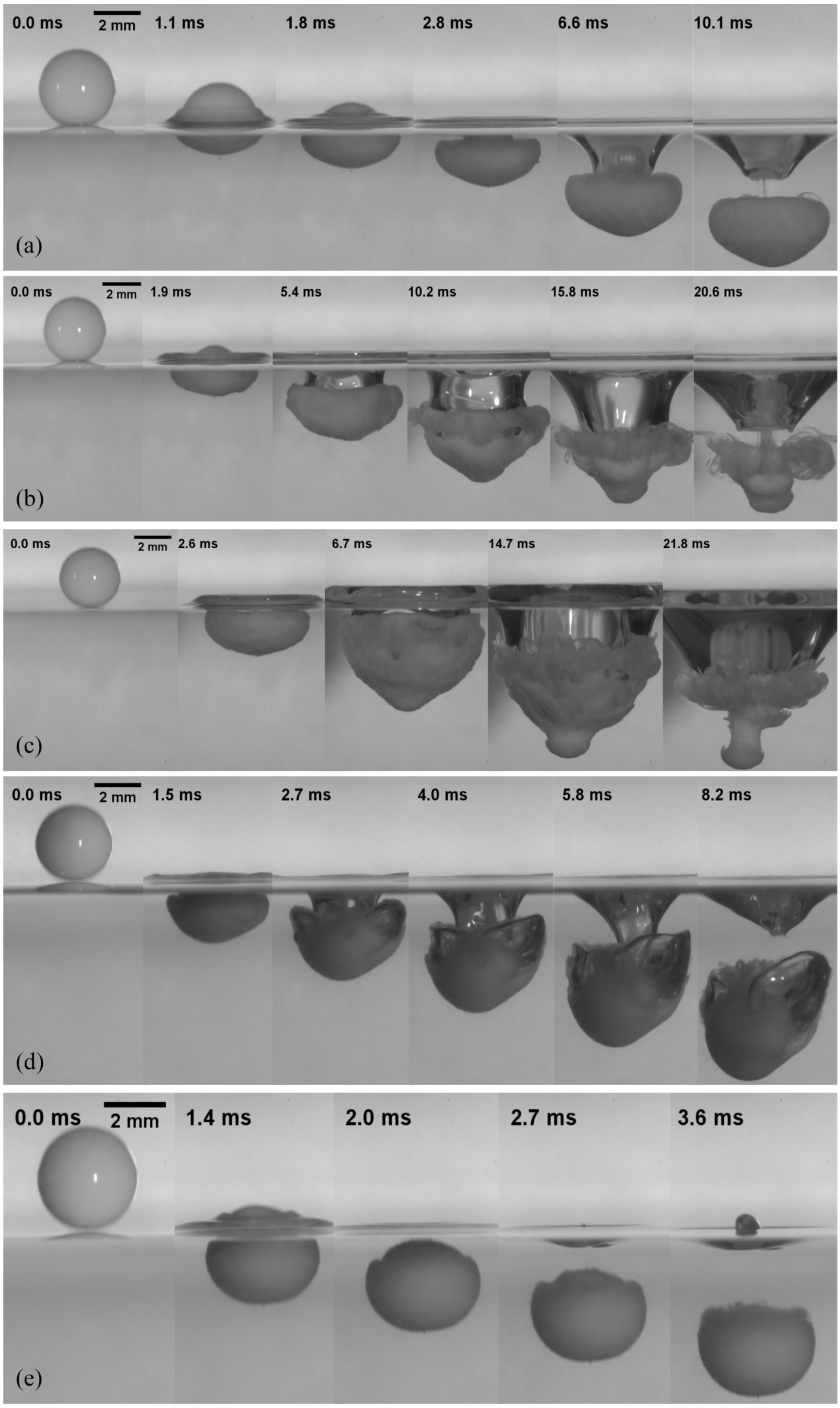

FIG. 3. Snapshots of the impact dynamics of cornstarch droplets on a deep water pool. (a) Liquid lump ($\phi = 36.8\%$, $u_0 = 0.85$ m/s), (b) partially attached ($\phi = 36.8\%$, $u_0 = 1.41$ m/s), (c) fully attached ($\phi = 36.8\%$, $u_0 = 2.07$ m/s), (d) wrapped bubble ($\phi = 41.6\%$, $u_0 = 1.45$ m/s), and (e) solid lump ($\phi = 47.5\%$, $u_0 = 1.39$ m/s).

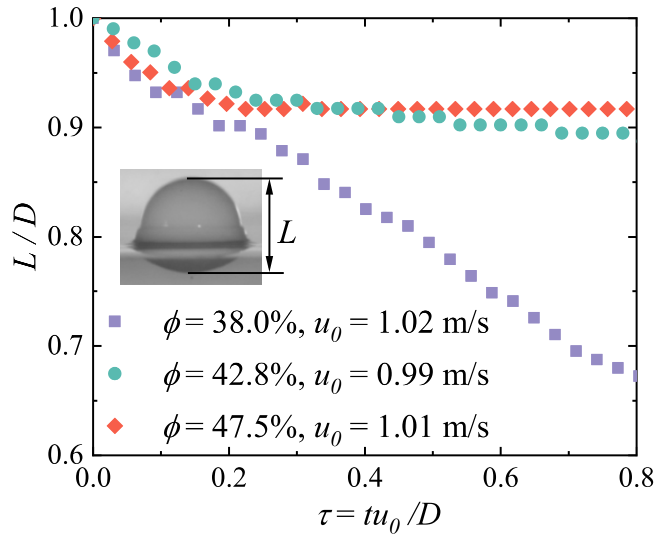

FIG. 4. Variations of the normalized height of droplet L/D with normalized time $\tau = tu_0/D$ for low ϕ ($= 38.0\%$), intermediate ϕ ($= 42.8\%$), and high ϕ ($= 47.5\%$) at $u_0 \approx 1.0$ m/s.

deformation similar to a Newtonian droplet. At $\phi = 42.8\%$, the deformation exhibits a stepwise behavior. This stepwise behavior is unique to suspension droplets impacting liquid pools and has not been reported for impacts on solid substrates. The difference may arise because the solid substrate imposes a rigid geometric constraint, whereas a liquid pool provides a compliant resistance without geometric constraint. At $\phi = 47.5\%$, L/D reaches a plateau shortly after contact, indicating that the deformation ends due to jamming. This observation is consistent with the abrupt cessation of deformation for suspension droplets impacting solid substrates [41,44].

The five impact phenomena are organized into a regime map in the space of particle volume fraction ϕ and Weber number $\mathrm{We} = \rho_d u_0^2 D/\sigma$ (the ratio between the inertia and the capillarity of the droplet), as shown in Fig. 5. The Weber number is selected as the dimensionless parameter to capture the dominance of capillarity of the pool surface at low u_0 and the dominance of inertia at

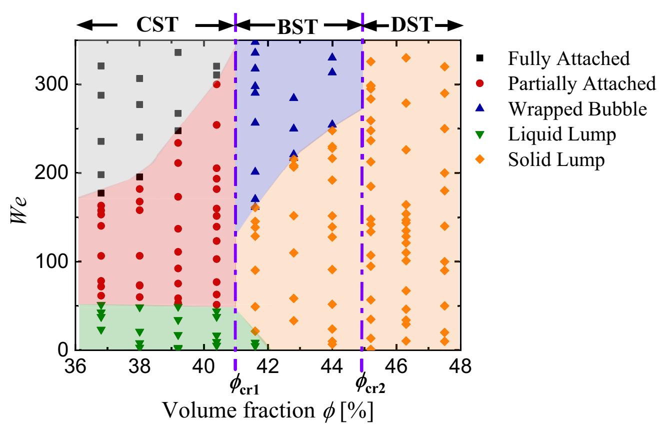

FIG. 5. Regime map of impact outcomes of cornstarch suspension droplets on a deep water pool in the We-ϕ space. Two dash-dotted lines denote two critical values of volume fractions $\phi_{\mathrm{cr1}} \approx 41\%$ and $\phi_{\mathrm{cr2}} \approx 45\%$ that divide the regime map into three regions based on experimental observations.

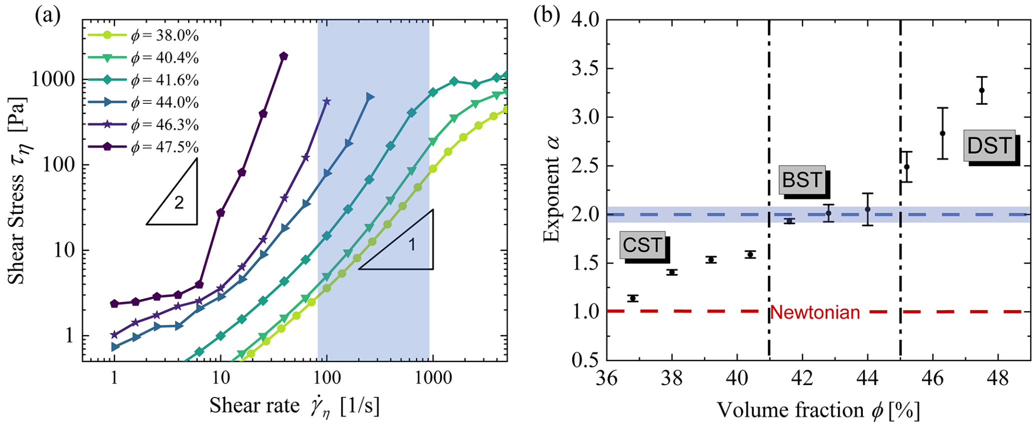

FIG. 6. (a) Rheological measurement of cornstarch suspensions with various volume fractions ϕ. (b) Variation of exponent α in rheological scaling law $\tau_\eta \propto \dot{\gamma}_\eta^\alpha$ with various volume fractions ϕ. The error bars represent the fitting uncertainty of α, obtained from the standard error of the power law fit of τ_η versus $\dot{\gamma}_\eta$ within the selected fitting range.

high u_0. Two critical volume fractions, $\phi_{cr1} \approx 41\%$ and $\phi_{cr2} \approx 45\%$, can be identified that divide the map into three regions, as shown by the dash-dotted lines. At low volume fraction ($\phi < \phi_{cr1}$), increasing We drives the transition from liquid lump to partially attached to fully attached. Both wrapped bubble and solid lump are observed in the intermediate ϕ range ($\phi_{cr1} < \phi < \phi_{cr2}$), while only solid lump is observed for $\phi > \phi_{cr2}$. Transition mechanisms will be identified to predict the transition boundaries in the following sections.

B. Rheological properties

The critical volume fractions are identified by characterizing the rheology of cornstarch suspensions in the range of ϕ tested in droplet impact experiments, as shown in Fig. 6(a). As ϕ increases, the shear thickening behavior becomes more prominent. For high volume fractions, no data were obtained at high shear rate due to jamming, which leads to patches of local solidification and slipperiness, resulting in the termination of the measurements [44]. The characteristic shear rate during the droplet impact process is estimated by $\dot{\gamma} = u_0/D$ [41,44] and ranges from 80 to 900 s^{-1}, which is marked by the shaded region in Fig. 6(a). The data in the shaded region is fitted to the power law $\tau_\eta \propto \dot{\gamma}_\eta^\alpha$ [55], where the exponent α is extracted and plotted against ϕ in Fig. 6(b). Since there is limited data in the shaded area for $\phi \geqslant 46.3\%$, the values of α are calculated based on the data outside the shaded region showing obvious shear thickening behavior. The exact values of α for these cases do not affect the categorization, as discussed below. The rheological behaviors of cornstarch suspensions are categorized based on Brown *et al.* [55,56]. $\alpha < 2$ corresponds to continuous shear thickening (CST), where the viscosity of the suspension increases gradually as the shear rate increases. discontinuous shear thickening (DST) occurs for $\alpha > 2$, where the viscosity of the suspension increases rapidly. Cases with $\alpha = 2$ are termed Bagnoldian shear thickening (BST), as they satisfy the Bagnoldian relationship [57]. Note that the term BST is used here to denote the $\alpha = 2$ rheology, while the indication of particle inertia is not relevant and thus not considered in the analysis of droplet impact dynamics. Based on these criteria and α values extracted from the shear rate range during droplet impact, cornstarch suspensions with $\phi < 41\%$ and $\phi > 45\%$ present CST and DST behaviors, respectively, while cornstarch suspensions with $41\% < \phi < 45\%$ are categorized as BST since α remains close to 2, which is consistent with the work by Boyer *et al.* [41]. The categorization is summarized in Table II and shown in Fig. 6(b) separated by the dash-dotted lines. The error bars in Fig. 6(b) represent the fitting uncertainty in α and show that the

TABLE II. Rheological categorization of the cornstarch suspensions.

Range of volume fraction ϕ	Values of α	Properties of fluid
$\phi < 41\%$	$1 < \alpha < 2$	Continuous shear thickening
$41\% < \phi < 45\%$	$\alpha = 2$	Bagnoldian shear thickening
$\phi > 45\%$	$\alpha > 2$	Discontinuous shear thickening

qualitative categorization is not affected by this uncertainty. Note that the divisions between CST, BST, and DST regions should not be interpreted as sharply defined phase boundaries or steplike transitions, but rather as rheological categories to highlight the evolution of rheological responses with ϕ and its correlation with the observed changes in the droplet impact regimes. Thus, two critical volume fractions: $\phi_{\mathrm{cr1}} \approx 41\%$ and $\phi_{\mathrm{cr2}} \approx 45\%$, can be identified to group the rheological behaviors of cornstarch suspensions into CST, BST, and DST regions. Remarkably, these critical volume fractions based on rheology coincide exactly with those identified from the regime map of droplet impact behaviors in Fig. 5. This alignment clearly shows that critical volume fractions are rheology controlled. The regimes of liquid lump, partially attached, and fully attached sit in the CST region, in which the impact behavior mostly resembles that of Newtonian droplet. In the DST region, only solid lump occurs due to impact induced jamming. In the BST region, both wrapped bubble and solid lump occur, which exhibit the transitional behavior between CST and DST. The We dependence in each rheological region will be discussed under Sec. IV.

IV. DISCUSSIONS

A. Continuous shear thickening region

In the CST region, the suspension exhibits slight shear thickening behavior, which does not significantly affect the interaction between the suspension droplets and the liquid pool. Thus, the observed regimes of liquid lump, partially attached, and fully attached resemble the phenomenon of a Newtonian droplet impact, with the snapshots shown in Fig. S4 in Supplemental Material [48]. To further quantify the similarity, the velocity of the bottom point of the mass from the droplet, u_{bot}, is measured and plotted against the impact velocity u_0, as shown in Fig. 7(a). The slope gives $\beta = u_{\mathrm{bot}}/u_0 = 0.61 \pm 0.009$, which is in good agreement with the theoretical value of $\beta_{N,\mathrm{theory}} = 0.59$ derived for Newtonian droplets impacting on liquid pools [58].

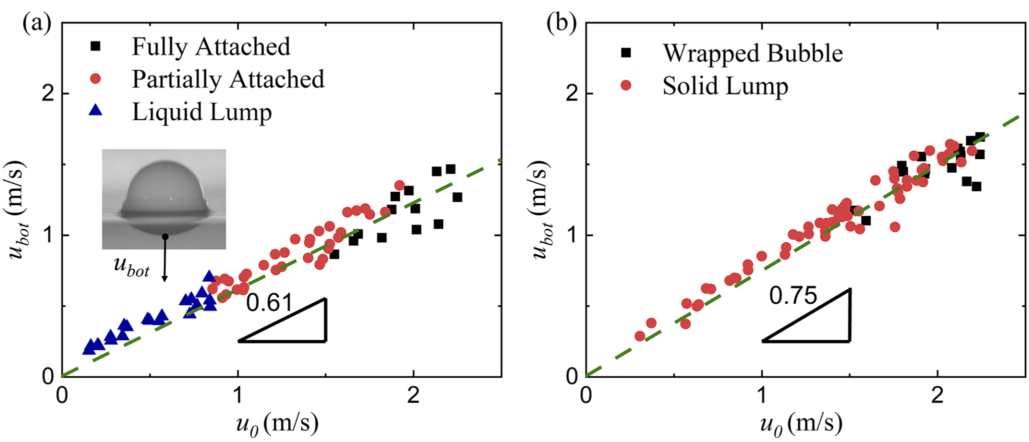

FIG. 7. (a) Variations of u_{bot} with respect to u_0 in CST region. (b) Variations of u_{bot} with respect to u_0 in BST and DST regions.

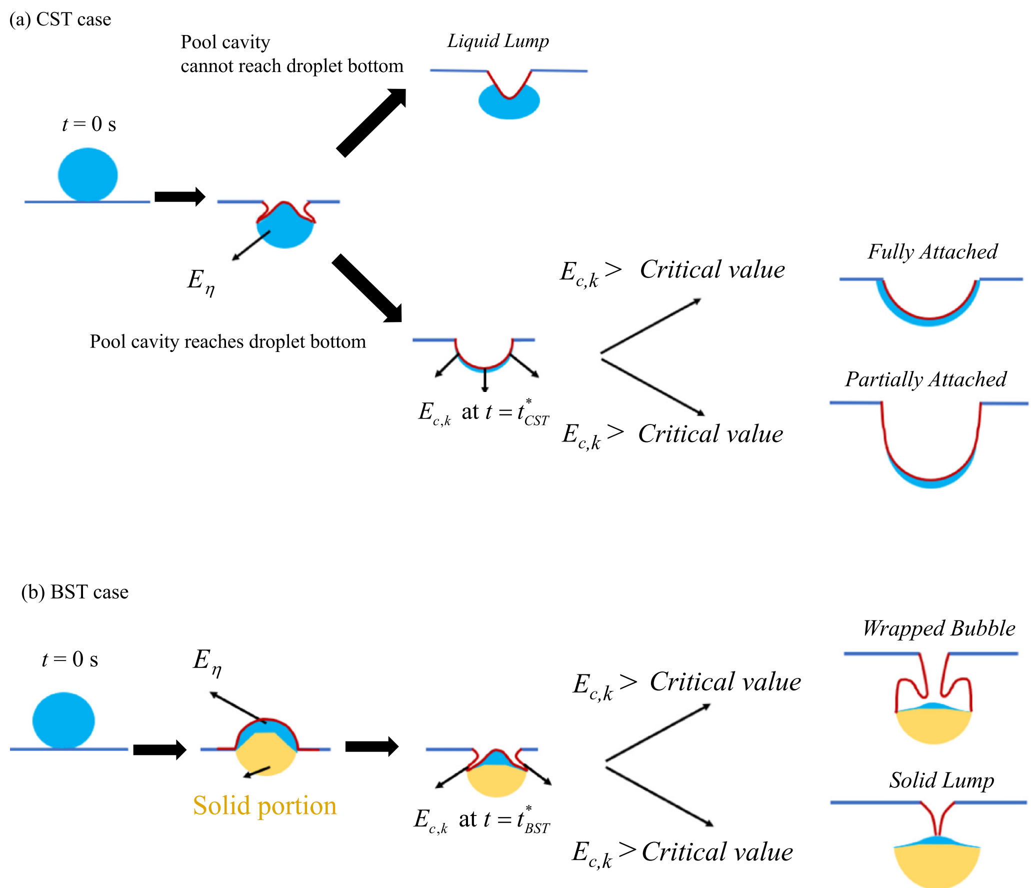

FIG. 8. (a) Impact process within the CST region: The transition criterion is controlled by the cavity kinetic energy $E_{c,k}$ at t^*_{CST}, the moment when the cavity catches up with the bottom of the droplet. (b) Impact process within the BST region: the transition criterion is controlled by $E_{c,k}$ at t^*_{BST}, the moment when the cavity aligns with the undisturbed pool surface where the cavity is nascent. Blue area: Liquid portion. Yellow area: Solid portion. Red line: Cavity surface, which is the top surface of the droplet. Blue line: Pool surface.

The transition between different regimes based on the droplet behaviors stems from the interaction between the cavity and the droplet. This interaction is best observed for water droplet impact, as shown in Fig. S4 in Supplemental Material [48], where the droplet is transparent in contrast to the opaque suspension droplet, while dyed to track the mass from the droplet. The observed interactions between the cavity and the Newtonian droplet will guide the analysis of the impact phenomenon of the suspension droplets in the CST region due to the similarity established above. Once a water droplet impacts on the surface at $t = 0$ s, it merges with the pool surface and the mass from the droplet descends through the pool. The cavity is formed by the top surface of the droplet as it expands downward. At low impact speed, capillarity controls the cavity expansion; thus the cavity exhibits a cone shape (Fig. S4(a) in Supplemental Material [48]). At high impact speed, inertia dominates and the cavity forms a spherical cap undergoing radial expansion (Fig. S4(c) in Supplemental Material [48]). As both the cavity and the mass from the droplet move downward, the cavity can catch up with the bottom of the mass from the droplet, which strongly disperses the mass into a thin film around the cavity as it expands. Figure 8(a) illustrates the origin of each suspension droplet impact regime and the transition criteria between them in the CST region. If the cavity does not have enough energy to catch up with the bottom of the mass from the droplet, then the droplet remains intact, falling as a cohesive mass in the liquid lump regime. The transition to the partially attached regime happens when the cavity just catches up with the bottom of the mass from the droplet when it reaches the maximum radius. Thus, at higher impact energy in the partially attached regime, the cavity only expands vertically as the mass from the droplet descends, forming a cylindrical cavity, where the mass from the droplet only covers part of the cavity. If the cavity obtains even higher energy, then it has enough energy left when the catch up happens, such that it continues to expand radially while fully dispersing the mass from the droplet to wrap around the entire cavity, resulting in the fully attached case.

The energy balance analysis is carried out during the impact process of the suspension droplets to quantify the critical We of the transitions:

$$E_{d,k} + E_{d,s} = E_{c,p} + E_{c,s} + E_{c,k} + E_{\eta}. \tag{1}$$

The left-hand side captures the energy of the droplet prior to impact: kinetic energy $E_{d,k} = \pi \rho_d D^3 u_0^2/12$ and surface energy $E_{d,s} = \sigma \pi D^2$. During impact, the energy is converted to the pool and the cavity: cavity kinetic energy $E_{c,k} = \pi \rho_p R_c^3 \dot{R}_c^2$, cavity surface energy $E_{c,s} = \sigma \pi R_c^2$, cavity potential energy $E_{c,p} = \pi \rho_p g R_c^4/4$, and viscous dissipation of the cornstarch suspension E_η due to droplet deformation. Here R_c is the radius of the cavity and $\dot{R}_c$ is the radial expansion speed of the cavity. As shown in Fig. 4, the droplet with a low volume fraction (CST region) undergoes continuous deformation while penetrating the liquid surface, resulting in viscous dissipation. However, at higher volume fractions (BST and DST regions), the droplet initially deforms before becoming jammed. During the prejamming stage, energy is dissipated through plastic deformation. Once a jammed state forms, particle motion is strongly constrained by geometric packing and a force-bearing contact network, and droplet deformation is largely hindered. In this stage, the cornstarch lump exhibits negligible deformation, so additional internal viscous dissipation is neglected. The evaluation of postimpact energy will be discussed at different characteristic times in each regime in the following sections.

1. Origins and transitions of liquid lump and partially attached

For the liquid lump–partially attached transition, if the cavity does not catch up with the bottom of the droplet at maximum depth, then it will never catch up, such that the mass from the droplet detaches afterwards to form the liquid lump, while the cavity retracts due to capillarity. Thus, the critical condition to distinguish the liquid lump from the partially attached regime is that the cavity just reaches the maximum depth $R_{\max}$ when it catches up with the bottom of the droplet at the critical moment t^*_{CST}. Since the cavity is essentially formed by the top surface of the droplet and travels at speed u_0, as shown in Fig. S2 in Supplemental Material [48], $t^*_{\mathrm{CST}} = (D + R_{\max})/u_0$. During this time, the bottom of the droplet travels a distance of $u_{\mathrm{bot}} t^*_{\mathrm{CST}}$, where $u_{\mathrm{bot}} = 0.61u_0$ from Fig. 7(a), which should be equal to $R_{\max}$ based on the transition criterion. Thus, the normalized critical maximum cavity depth is $\tilde{R}^{\mathrm{cr}}_{\max} = 1.564$. At this critical moment, $E_{c,k}$ is negligible since the cavity reaches the maximum depth. As discussed before and shown in Fig. S4(a) in Supplemental Material [48], at such low We, the cavity has a cone or cylindrical shape which does not strongly interact with the droplet. Thus, viscous dissipation E_η in the mass from the droplet can be neglected. The normalized energy balance equation Eq. (1) becomes

$$\frac{\mathrm{We}}{12} = \frac{\rho^* \tilde{R}^4_{\max}}{2\tilde{l}^2_{c,d}} + \left(\tilde{R}^2_{\max} - 1\right), \tag{2}$$

where $\rho^* = \rho_p/\rho_d$ (ρ_p, density of the pool), $\tilde{R}_{\max} = R_{\max}/D$, and $\tilde{l}_{c,d} = \sqrt{2\sigma/\rho_d g}/D = 1.00$ is the normalized capillary length. Plugging $\tilde{R}^{\mathrm{cr}}_{\max} = 1.564$ into Eq. (2) gives the critical We for the liquid lump–to–partially attached transition: $\mathrm{We}_{\mathrm{cr},l-p} = 39.39$. The prediction of $\mathrm{We}_{\mathrm{cr},l-p}$ does not involve any fitting parameters and cleanly separates the two regimes, as shown in Fig. 9(a). Note that $\mathrm{We}_{\mathrm{cr},l-p}$ is independent of ϕ, highlighting that viscous dissipation does not play an important

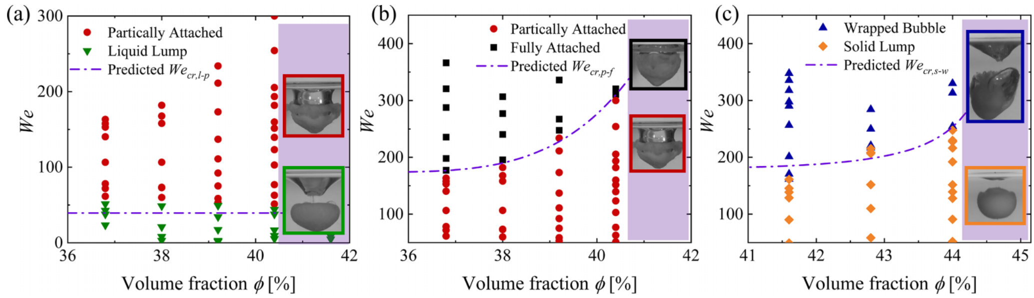

FIG. 9. (a) Comparison of the predicted transition boundary $\mathrm{We}_{\mathrm{cr},l-p}$ with the experimental data for liquid lump and partially attached cases. (b) Comparison of the predicted transition boundary $\mathrm{We}_{\mathrm{cr},p-f}$ with the experimental data for fully attached and partially attached cases. (c) Comparison of the predicted transition boundary $\mathrm{We}_{\mathrm{cr},s-w}$ with the experimental data for the wrapped bubble and solid lump cases.

role at such low impact speed, where the cavity does not gain enough energy to interact with the droplet to introduce strong flows.

In summary, if $\mathrm{We} > \mathrm{We}_{\mathrm{cr},l-p} = 39.39$, then the cavity reaches the bottom of the droplet and its subsequent expansion partially breaks up the cornstarch lump, producing the partially attached regime. Otherwise, the cavity does not have enough energy to interact with the droplet, and thus the droplet remains intact and falls as a cohesive mass in the liquid lump regime.

2. *Origins and transitions of partially attached and fully attached*

As We increases, the cavity gains more energy to disperse the mass from the droplet to a thin film that wraps around the cavity. On the other hand, higher impact inertia leads to stronger internal flow in the suspension droplet, which results in higher viscous dissipation, reducing the energy transferred to the cavity, and thus the mass from the droplet is not fully dispersed. Viscous dissipation becomes important at higher We for two reasons: (i) *shear thickening*, which increases the effective viscosity with higher deformation rate, and (ii) *geometric thinning* as higher We produces a thinner layer and therefore a larger characteristic deformation rate (inversely proportional to the layer thickness). The transition between the partially attached and the fully attached cases is thus controlled by the competition between the cavity energy and the viscous dissipation in the suspension. If viscous dissipation in the suspension removes a substantial fraction of the initial cavity kinetic energy, then cavity expansion is suppressed and the cornstarch lump cannot fully break up and attach to the cavity, leading to the partially attached case. On the other hand, the cavity has so much energy compared to viscous dissipation that the cavity evolves largely unimpeded, and the impact dynamics resembles that of the Newtonian case, where the mass from the droplet is fully attached to the cavity interface (Fig. S4 in Supplemental Material [48]).

The transition boundary is evaluated by comparing the initial cavity energy and the viscous dissipation as the droplet deforms. The initial cavity energy is evaluated by the energy balance model [Eq. (1)] when the cavity is nascent, and thus $E_{c,s}$ and $E_{c,p}$ are negligible. $E_{d,s}$ is negligible as We > 100. Thus, the initial cavity energy scales as the kinetic energy of the droplet: $E_{c,k,0} \propto \rho_d D^3 u_0^2$. Viscous dissipation is estimated by $E_\eta = t^* \int d^3 r \tau_\eta \dot{\gamma}$, in which viscous stress $\tau_\eta = k_{\mathrm{CST}}(\phi)\dot{\gamma}^\alpha$. The characteristic timescale is selected as the inertia timescale, $t^* = D/u_0$, to represent the duration of droplet deformation. The shear rate $\dot{\gamma} = u_0/D$. Thus $E_\eta \propto V_d k_{\mathrm{CST}}(\phi) u_0^\alpha / D^\alpha$. Note that $E_{c,k,0} \propto u_0^2$, which grows faster with impact velocity than E_η since $\alpha < 2$, which indicates that at high-enough u_0, inertia dominates such that the droplet impact behavior resembles the Newtonian droplet impact. The transition between partially attached and fully attached can be obtained from the balance

$E_{c,k,0} \sim E_\eta$:

$$u_{0,\mathrm{cr},p-f} \sim \left(\frac{k_{\mathrm{CST}}(\phi)}{\rho_d D^\alpha}\right)^{\frac{1}{2-\alpha}} \tag{3}$$

and

$$\mathrm{We}_{\mathrm{cr},p-f} = \frac{\rho_d D u_{0,\mathrm{cr},p-f}^2}{\sigma} \propto k_{\mathrm{CST}}(\phi)^{\frac{2}{2-\alpha}}. \tag{4}$$

By adopting $\alpha = 1.5$ in the CST region ($1 < \alpha < 2$), the critical Weber number simplifies to $\mathrm{We}_{\mathrm{cr},p\text{-}f} \propto k_{\mathrm{CST}}(\phi)^4$. $k_{\mathrm{CST}}(\phi)$ is extracted from rheological measurements [Fig. 6(a)] via the constitutive relation $\tau_\eta = k_{\mathrm{CST}}(\phi)\dot{\gamma}^{1.5}$. As evidenced in Fig. S6(a) in Supplemental Material [48], $k_{\mathrm{CST}}(\phi)$ exhibits a linear dependence on ϕ, captured by $k_{\mathrm{CST}}(\phi) = a\phi - b$ with best-fit parameters $a = 0.107 \pm 0.003$ Pa s$^{1.5}$ and $b = 0.037 \pm 0.001$ Pa s$^{1.5}$. To provide a semiempirical relation for practical use, the transition boundary is written as $\mathrm{We}_{\mathrm{cr},p-f} = c_1 + c_2 k_{\mathrm{CST}}(\phi)^4$. c_1 is dimensionless and accounts for energy-loss terms not explicitly included in the simplified scaling analysis, such as the conversion of the initial droplet energy into cavity motion, wave generation, and other dissipative processes, and c_2 accounts for prefactors omitted in the scaling estimate.

The transition boundary fitted with $c_1 = 173.7 \pm 5.9$, $c_2 = 9.1 \times 10^{10} \pm 7.2 \times 10^9$ (Pa s$^{1.5}$)$^{-4}$ is shown in Fig. 9(b). The predicted scaling $\mathrm{We}_{\mathrm{cr},p\text{-}f} \propto k_{\mathrm{CST}}(\phi)^4$ captures the experimental transition boundary well. As ϕ increases, $\mathrm{We}_{\mathrm{cr},p-f}$ increases, which requires higher droplet inertia to overcome the stronger viscous dissipation for the cavity to disperse the mass from the droplet to form the fully attached case.

B. Bagnoldian shear thickening region

In the BST ($41.0\% < \phi < 45.0\%$) region with $\tau_\eta \propto \dot{\gamma}_\eta^2$, the impact phenomena wrapped bubble and solid lump differ qualitatively from those in the CST region in terms of both the droplet and cavity dynamics. The mass from the droplet stays mostly together without being dispersed as in the CST region. The cavity dynamics does not resemble that of Newtonian droplet impact as in the CST region; instead, it either has limited expansion and is pinched off into bubbles in the wrapped bubble regime or does not occur in the solid lump regime. This difference stems from the Bagnoldian shear thickening behavior $\tau_\eta \propto \dot{\gamma}_\eta^2$. As observed in similar systems with BST behavior, such as surface flow of granular materials [59, 60], stepwise deformation as quantified by the droplet height at $\phi = 42.8\%$ is observed, as shown in Fig. 4, further confirming the significant role of suspension rheology in impact phenomenon. Furthermore, in contrast to the CST region, the slope $\beta = u_{\mathrm{bot}}/u_0 = 0.75$ deviates from the theoretical value of $\beta_{N,\mathrm{theory}} = 0.59$ for Newtonian droplets impacting on liquid pools [58], as shown in Fig. 7(b). The combination of high viscous dissipation and strong resistance between particles in the BST region stabilizes the shape of the droplet and suppresses the formation and expansion of the cavity.

To further demonstrate that the phenomena come from the BST behavior instead of a simple high viscosity effect, droplet impact experiments with glycerol-water mixture whose viscosity matches that in the BST region are shown in Fig. S5 in Supplemental Material [48]. Neither bubble entrapment nor suppressed cavity is observed in the same range of We, and the glycerol-water droplets continuously deform during impact, in contrast to the stepwise deformation of the suspension droplets. In addition, the bottom section of the suspension droplets remains invariant in shape and only the upper section breaks, as shown in Fig. 3(d). This partial deformation resembles the coexisting liquid and solid phases observed for the impact of suspension droplets on solid substrates [44]. Thus, the coexisting phase in the BST region leads to the wrapped bubble: The top liquid phase interacts with the pool to form the cavity, while the bottom solid phase impedes the expansion of the cavity, such that the narrowing cavity neck pinches off into bubbles as the droplet descends. At smaller We, the cavity does not have enough energy to pinch off, forming the solid lump. Thus, the transition criterion between solid lump and wrapped bubble is whether the cavity can grow large enough to pinch off when the cavity starts to evolve.

To quantify the transition boundary, the energy balance model is evaluated at the characteristic time t^*_{BST}, when the top surface of the droplet aligns with the undisturbed pool surface. Since the cavity size $\tilde{R}_c = R_c/D$ is negligible at t^*_{BST} as shown in Fig. 8(b), the surface energy $E_{c,s}$ and the potential energy $E_{c,p}$ of the cavity can be neglected [61]. Neglecting the droplet surface energy $E_{d,s}$ at We > 100, the energy balance gives $E_{c,k} = E_{d,k} - E_\eta$. Viscous dissipation $E_\eta = t^*_{\mathrm{BST}} \int d^3 r \tau_\eta \dot{\gamma}$ is modeled by considering only the liquid portion of the coexisting phase for the mass transferred from the droplet. As shown in Fig. 8(b), droplet deformation occurs exclusively in the early stage immediately following impact, after which it ceases. Consequently, viscous dissipation is attributed solely to the deformation stage and ceases once the deformation is arrested by particle jamming. This motivates the introduction of the dissipation fraction inside the droplet θ, which gives $E_{c,k} = E_{d,k} - \theta t^*_{\mathrm{BST}} \int d^3 r \tau_\eta \dot{\gamma}$. θ serves as a fitting parameter in this equation. In addition, $k_{\mathrm{BST}}(\phi) = 5.3 \times 10^{-9}(1 - \phi/0.52)^{-7.69}$ Pa s^2 is fitted from the rheology measurement as shown in Fig. S6(b) in Supplemental Material [48].

The transition criterion is given by whether there is enough remaining kinetic energy $E_{c,k} = E_{c,k,\mathrm{cr}}$ for the cavity to pinch off to form the wrapped bubble. Note that unlike the transition from partially attached to fully attached in the CST region, where the expansion of the cavity competes against viscous dissipation throughout the cavity development, the viscous dissipation in the BST region happens at the initial stage to reduce the energy transferred to the cavity, and the cavity expansion is confined by the jammed solid phase. Due to the challenge in theoretically predicting $E_{c,k,\mathrm{cr}}$, it is absorbed into the fitting parameters when carrying out the energy balance to find the semiempirical transition $\mathrm{We}_{\mathrm{cr},s-w}$,

$$\mathrm{We}_{\mathrm{cr},s-w} = \frac{c_3}{(1/12 - c_4\, k_{\mathrm{BST}}(\phi))}, \tag{5}$$

shown as the dash-dotted line in Fig. 9(c) with $c_3 = 177.6 \pm 11.4$ and $c_4 = 31.7 \pm 6.8$ (Pa s^2)$^{-1}$. Here c_3 accounts for the finite cavity energy threshold required for bubble pinch-off, whereas c_4 absorbs the dissipation fraction θ, geometric factors, and other prefactors omitted in the scaling estimate. The fitted boundary agrees well with the experimental data and captures the increase of $\mathrm{We}_{\mathrm{cr},s-w}$ with ϕ: Higher ϕ leads to stronger viscous dissipation and therefore requires larger inertia to generate a cavity large enough to pinch off to form the wrapped bubble.

C. Discontinuous shear thickening region

At high volume fraction ($\phi > 45.0\%$), the wrapped bubble regime vanishes and only solid lump occurs. In this DST dominated region, particle motion is restricted, causing the droplet to behave like a solid. As shown in Fig. 4 for $\phi = 47.5\%$, after an initial deformation, the height of the droplet reaches a plateau, indicating impact-induced jamming [36,37,62]. Further evidence of impact-induced jamming comes from cavity suppression, as shown in Fig. 3(e), which resembles the case of a hydrophilic solid sphere impacting a liquid pool [51]. Therefore, although the droplet remains liquid prior to impact, it solidifies during impact. Further discussion of the phase transition during the impact will be detailed in our future work.

From the energy point of view, the cavity energy E_c scales as the droplet kinetic energy $E_{d,k} = \pi \rho_d D^3 u_0^2/12$, where the viscous dissipation $E_\eta \propto V_d k_{\mathrm{DST}}(\phi) u_0^\alpha / D^\alpha$ with $\alpha > 2$. Thus, with increasing u_0, E_η increases much faster than E_c. Therefore, in the DST region, even at high u_0, the large E_c gained from droplet inertia can still be dissipated by viscous dissipation E_η due to strong shear thickening, leading to diminished cavity, such that the wrapped bubble disappears in the DST region.

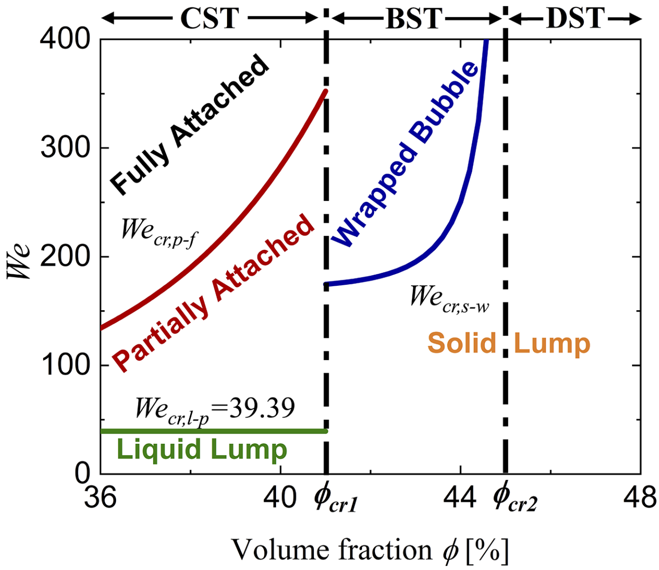

FIG. 10. Regime map with predicted Weber number for the transition boundaries of cornstarch droplet impacting on a liquid pool. $\mathrm{We}_{\mathrm{cr},l-p} = 39.39$; $\mathrm{We}_{\mathrm{cr},p-f} = 173.7 + 9.1 \times 10^{10} k_{\mathrm{CST}}(\phi)^4$, where $k_{\mathrm{CST}}(\phi) = 0.107\phi - 0.037$ Pa s$^{1.5}$; $\mathrm{We}_{\mathrm{cr},s-w} = 177.6/(1/12–31.7k_{\mathrm{BST}}(\phi))$, where $k_{\mathrm{BST}}(\phi) = 5.3 \times 10^{-9}(1–\phi/0.52)^{-7.69}$ Pa s^2. The comparison between the experimental data and the predicted transition boundaries is shown in Fig. 9.

V. CONCLUSION

In this work, we experimentally investigated the impact dynamics of cornstarch suspension droplets on a deep water pool. We identified a regime map in the We-ϕ space consisting of five distinct impact regimes (Fig. 5) and proposed theoretical predictions for the transition boundaries as summarized in Fig. 10. Rheology tests of the cornstarch suspension revealed that the two critical volume fractions $\phi_{\mathrm{cr},1} \approx 41\%$ and $\phi_{\mathrm{cr},2} \approx 45\%$, which divide the regime map into three regions, are controlled by the transition of the suspension behavior from CST to BST to DST, based on the value of α in the power law $\tau_\eta \propto \dot{\gamma}^\alpha$. In the CST region ($1 < \alpha < 2$, $\phi < \phi_{\mathrm{cr},1}$) liquid lump, partially attached, and fully attached occur, where the cavity dynamics closely resembles that of Newtonian droplet impact, and the weak viscosity variation modifies how particles are dispersed by the cavity expansion. The BST region ($\alpha = 2$, $\phi_{\mathrm{cr},1} < \phi < \phi_{\mathrm{cr},2}$) contains wrapped bubble and solid lump regimes, both fundamentally different from the impact dynamics of Newtonian droplets. The coexistence of the liquid and solid phases in the droplet during impact leads to the wrapped bubble, where, at low We, solid lump occurs due to the jamming of the particles. In the DST region ($\alpha > 2$, $\phi > \phi_{\mathrm{cr},2}$), only solid lump occurs, where impact-induced jamming occurs at all We, causing the droplet to behave like a solid sphere.

We further quantified the critical Weber number for each transition boundary in the CST and BST regions (summarized in Fig. 10) by carrying out energy balance analysis during the droplet impact, where the coupling between the cavity and non-Newtonian behavior of the suspension plays a critical role. The scaling predictions of the transition boundaries agree well with the experimental data by capturing the underlying physics. We further provided semiempirical expressions that quantitatively describe the transition boundaries for practical usage and offer a systematic foundation for further studies of suspension droplets impact on liquid surfaces. Our study fills a research gap on the impact dynamics of suspension droplets on a liquid pool and deepens our understanding of the interplay between impact dynamics, cavity evolution, and rheological properties, providing practical guidance for engineering applications such as controlling cavity formation, improving precision in three-dimensional printing, and optimizing medical storage.

ACKNOWLEDGMENTS

The authors acknowledge NSF funding support under Award No. CMMI-2227985. The authors thank Prof. Sara Hashmi and Dr. Saeed Alborzi for their support with rheological measurements.

DATA AVAILABILITY

Most data supporting the findings of this article are presented in the figures. Data are available from the corresponding author upon reasonable request.

---

[1] A. L. Yarin, Drop impact dynamics: Splashing, spreading, receding, bouncing, Annu. Rev. Fluid Mech. **38**, 159 (2006).
[2] M. Rein, Phenomena of liquid drop impact on solid and liquid surfaces, Fluid Dyn. Res. **12**, 61 (1993).
[3] K. L. Pan and C. K. Law, Dynamics of droplet–film collision, J. Fluid Mech. **587**, 1 (2007).
[4] Z. Che and O. K. Matar, Impact of droplets on immiscible liquid films, Soft Matter **14**, 1540 (2018).
[5] S. Kim, Z. Wu, E. Esmaili, J. J. Dombroskie, and S. Jung, How a raindrop gets shattered on biological surfaces, Proc. Natl. Acad. Sci. USA **117**, 13901 (2020).
[6] S. Gart, J. E. Mates, C. M. Megaridis, and S. Jung, Droplet impacting a cantilever: A leaf-raindrop system, Phys. Rev. Appl. **3**, 044019 (2015).
[7] S. Bagchi, S. Basu, S. Chaudhuri, and A. Saha, Penetration and secondary atomization of droplets impacted on wet facemasks, Phys. Rev. Fluids **6**, 110510 (2021).
[8] E. Dressaire, A. Sauret, F. Boulogne, and H. A. Stone, Drop impact on a flexible fiber, Soft Matter **12**, 200 (2016).
[9] M. Pack, H. Hu, D. Kim, Z. Zheng, H. Stone, and Y. Sun, Failure mechanisms of air entrainment in drop impact on lubricated surfaces, Soft Matter **13**, 2402 (2017).
[10] P. Tsai, S. Pacheco, C. Pirat, L. Lefferts, and D. Lohse, Drop impact upon micro-and nanostructured superhydrophobic surfaces, Langmuir **25**, 12293 (2009).
[11] M. Guémas, Á. G. Marín, and D. Lohse, Drop impact experiments of non-Newtonian liquids on micro-structured surfaces, Soft Matter **8**, 10725 (2012).
[12] U. Jain, M. Jalaal, D. Lohse, and D. van der Meer, Deep pool water-impacts of viscous oil droplets, Soft Matter **15**, 4629 (2019).
[13] X. Tang, A. Saha, C. K. Law, and C. Sun, Bouncing drop on liquid film: Dynamics of interfacial gas layer, Phys. Fluids **31**, 013304 (2019).
[14] D. Richard, C. Clanet, and D. Quéré, Contact time of a bouncing drop, Nature (London) **417**, 811 (2002).
[15] J. De Ruiter, R. Lagraauw, D. Van Den Ende, and F. Mugele, Wettability-independent bouncing on flat surfaces mediated by thin air films, Nat. Phys. **11**, 48 (2015).
[16] J. M. Kolinski, L. Mahadevan, and S. M. Rubinstein, Drops can bounce from perfectly hydrophilic surfaces, Europhys. Lett. **108**, 24001 (2014).
[17] X. Tang, A. Saha, C. K. Law, and C. Sun, Bouncing-to-merging transition in drop impact on liquid film: Role of liquid viscosity, Langmuir **34**, 2654 (2018).
[18] J. Zou, P. F. Wang, T. R. Zhang, X. Fu, and X. Ruan, Experimental study of a drop bouncing on a liquid surface, Phys. Fluids **23**, 044101 (2011).
[19] Z. He, H. Tran, and M. Y. Pack, Drop bouncing dynamics on ultrathin films, Langmuir **37**, 10135 (2021).
[20] J. Lee, N. Laan, K. G. de Bruin, G. Skantzaris, N. Shahidzadeh, D. Derome, J. Carmeliet, and D. Bonn, Universal rescaling of drop impact on smooth and rough surfaces, J. Fluid Mech. **786**, R4 (2016).

[21] G. Lagubeau, M. A. Fontelos, C. Josserand, A. Maurel, V. Pagneux, and P. Petitjeans, Spreading dynamics of drop impacts, J. Fluid Mech. **713**, 50 (2012).
[22] I. V. Roisman, R. Rioboo, and C. Tropea, Normal impact of a liquid drop on a dry surface: Model for spreading and receding, Philos. Trans. Roy. Soc. A **458**, 1411 (2002).
[23] N. Laan, K. G. de Bruin, D. Bartolo, C. Josserand, and D. Bonn, Maximum diameter of impacting liquid droplets, Phys. Rev. Appl. **2**, 044018 (2014).
[24] S. Wildeman, C. W. Visser, C. Sun, and D. Lohse, On the spreading of impacting drops, J. Fluid Mech. **805**, 636 (2016).
[25] X. Tang, A. Saha, C. Sun, and C. K. Law, Spreading and oscillation dynamics of drop impacting liquid film, J. Fluid Mech. **881**, 859 (2019).
[26] M. Mani, S. Mandre, and M. P. Brenner, Events before droplet splashing on a solid surface, J. Fluid Mech. **647**, 163 (2010).
[27] L. Xu, W. W. Zhang, and S. R. Nagel, Drop splashing on a dry smooth surface, Phys. Rev. Lett. **94**, 184505 (2005).
[28] L. V. Zhang, P. Brunet, J. Eggers, and R. D. Deegan, Wavelength selection in the crown splash, Phys. Fluids **22**, 122105 (2010).
[29] D. W. Murphy, C. Li, V. d'Albignac, D. Morra, and J. Katz, Splash behaviour and oily marine aerosol production by raindrops impacting oil slicks, J. Fluid Mech. **780**, 536 (2015).
[30] L. Yang, Z. Li, T. Yang, Y. Chi, and P. Zhang, Experimental study on droplet splash and receding breakup on a smooth surface at atmospheric pressure, Langmuir **37**, 10838 (2021).
[31] G. Juarez, T. Gastopoulos, Y. Zhang, M. L. Siegel, and P. E. Arratia, Splash control of drop impacts with geometric targets, Phys. Rev. E **85**, 026319 (2012).
[32] X. Peng, T. Wang, K. Sun, and Z. Che, Droplet splashing during the impact on liquid pools of shear-thinning fluids with yield stress, Phys. Fluids **33**, 112106 (2021).
[33] J. Liu, S. Z. Qiao, H. Liu, J. Chen, A. Orpe, D. Zhao, and G. Q. Lu, Extension of the Stöber method to the preparation of monodisperse resorcinol–formaldehyde resin polymer and carbon spheres, Angew. Chem. **123**, 6069 (2011).
[34] J. Mewis and N. J. Wagner, *Colloidal Suspension Rheology* (Cambridge University Press, Cambridge, UK, 2012).
[35] J. F. Morris, Toward a fluid mechanics of suspensions, Phys. Rev. Fluids **5**, 110519 (2020).
[36] D. Bi, J. Zhang, B. Chakraborty, and R. P. Behringer, Jamming by shear, Nature (London) **480**, 355 (2011).
[37] S. R. Waitukaitis and H. M. Jaeger, Impact-activated solidification of dense suspensions via dynamic jamming fronts, Nature (London) **487**, 205 (2012).
[38] E. Han, I. R. Peters, and H. M. Jaeger, High-speed ultrasound imaging in dense suspensions reveals impact-activated solidification due to dynamic shear jamming, Nat. Commun. **7**, 12243 (2016).
[39] E. Han, L. Zhao, N. Van Ha, S. T. Hsieh, D. B. Szyld, and H. M. Jaeger, Dynamic jamming of dense suspensions under tilted impact, Phys. Rev. Fluids **4**, 063304 (2019).
[40] P. Shah and M. M. Driscoll, Drop impact dynamics of complex fluids: A review, Soft Matter **20**, 4839 (2024).
[41] F. Boyer, E. Sandoval-Nava, J. H. Snoeijer, J. F. Dijksman, and D. Lohse, Drop impact of shear thickening liquids, Phys. Rev. Fluids **1**, 013901 (2016).
[42] V. Bertola and M. D. Haw, Impact of concentrated colloidal suspension drops on solid surfaces, Powder Technol. **270**, 412 (2015).
[43] H. Cao, R. Hu, Y.-F. Chen, C. Gui, Z. Yang, *et al.*, Regulating droplet impact dynamics of nanoparticle suspension: Phenomena, mechanisms, and implications, Phys. Fluids **36**, 012002 (2024).
[44] P. Shah, S. Arora, and M. M. Driscoll, Coexistence of solid and liquid phases in shear jammed colloidal drops, Commun. Phys. **5**, 222 (2022).
[45] A. Fall, F. Bertrand, G. Ovarlez, and D. Bonn, Shear thickening of cornstarch suspensions, J. Rheol. **56**, 575 (2012).
[46] R. I. Tanner, Review article: Aspects of non-colloidal suspension rheology, Phys. Fluids **30**, 101301 (2018).

[47] E. Han, N. V. Ha, and H. M. Jaeger, Measuring the porosity and compressibility of liquid-suspended porous particles using ultrasound, Soft Matter **13**, 3506 (2017).
[48] See Supplemental Material at http://link.aps.org/supplemental/10.1103/fxw2-38g4 for details on the volume-fraction calculation, image measurements, regime classification, reference impact dynamics of water droplet and glycerol-water droplet, and rheological fitting procedure.
[49] C. E. Stauffer, The measurement of surface tension by the pendant drop technique, J. Phys. Chem. **69**, 1933 (1965).
[50] E. Y. Arashiro and N. R. Demarquette, Use of the pendant drop method to measure interfacial tension between molten polymers, Mater. Res. **2**, 23 (1999).
[51] C. Duez, C. Ybert, C. Clanet, and L. Bocquet, Making a splash with water repellency, Nat. Phys. **3**, 180 (2007).
[52] T. T. Truscott, B. P. Epps, and J. Belden, Water entry of projectiles, Annu. Rev. Fluid Mech. **46**, 355 (2014).
[53] J. M. Aristoff, T. T. Truscott, A. H. Techet, and J. W. Bush, The water entry of decelerating spheres, Phys. Fluids **22**, 032102 (2010).
[54] H. Marschall, K. A. Mørch, A. Keller, and M. Kjeldsen, Cavitation inception by almost spherical solid particles in water, Phys. Fluids **15**, 545 (2003).
[55] E. Brown and H. M. Jaeger, Shear thickening in concentrated suspensions: Phenomenology, mechanisms and relations to jamming, Rep. Prog. Phys. **77**, 046602 (2014).
[56] J. F. Morris, Shear thickening of concentrated suspensions: Recent developments and relation to other phenomena, Annu. Rev. Fluid Mech. **52**, 121 (2020).
[57] R. A. Bagnold, Experiments on a gravity-free dispersion of large solid spheres in a Newtonian fluid under shear, Proc. R. Soc. Lond. A **225**, 49 (1954).
[58] B. D. Fudge, R. Cimpeanu, and A. A. Castrejón-Pita, Dipping into a new pool: The interface dynamics of drops impacting onto a different liquid, Phys. Rev. E **104**, 065102 (2021).
[59] S. Douady, B. Andreotti, A. Daerr, and P. Cladé, From a grain to avalanches: On the physics of granular surface flows, C. R. Phys. **3**, 177 (2002).
[60] K.-L. Lee and T.-Y. Yeh, Mesoscale avalanche size underpins the rheology of granular yielding, Proc. Natl. Acad. Sci. USA **122**, e2516426122 (2025).
[61] V. Lherm, R. Deguen, T. Alboussière, and M. Landeau, Rayleigh–Taylor instability in impact cratering experiments, J. Fluid Mech. **937**, A20 (2022).
[62] A. J. Liu and S. R. Nagel, Jamming is not just cool any more, Nature (London) **396**, 21 (1998).